https://doi.org/10.5194/egusphere-2026-1330
Preprint. Discussion started: 18 March 2026

Development of iron-mediated molecular chlorine chemistry in GEOS-Chem: model description, evaluation and global atmospheric implication

Jing Chen[1], Xianyi Sun[1], Chuang Qin[1], Jie Li[1], Qianjie Chen[2], Xiao Fu[1]

[1] Institute of Environment and Ecology, Tsinghua Shenzhen International Graduate School, Tsinghua University, Shenzhen 518055, China
[2] Department of Civil and Environmental Engineering, The Hong Kong Polytechnic University, Hong Kong SAR 999077, China

Correspondence to: Xiao Fu (fu.xiao@sz.tsinghua.edu.cn)

Abstract. Molecular chlorine (Cl_2) plays a significant role in shaping atmospheric oxidative capacity (AOC), yet global models tend to underestimate Cl_2 concentrations due to incomplete representations of its formation pathways. Here, we implement an iron(Fe)-mediated Cl_2 formation mechanism into the GEOS-Chem model, explicitly representing the dynamic solubility of iron driven by acid processing, organic complexation, and mineralogical variability. The updated mechanism substantially improves the model performance for tropospheric Cl_2, increasing correlation coefficient with observations from 0.55 to 0.88 relative to the Base simulation (without Fe-Cl mechanism). Global surface mean Cl_2 concentration increases about fivefold (from 0.4 to 2.2 pptv) which strengthens radical propagation, leading to approximately threefold and fourfold rise in global Cl and ClO radicals, respectively. These radical perturbations further result in pronounced spatial heterogeneity in AOC. While global mean OH decreases by 5.7% due to removal of O_3 by Cl and conversion of HO*x* to ClO*x*, eastern China experiences concurrent increases in O_3 and OH (up to 14%), as enhanced RO_2 formation from Cl-accelerated VOCs oxidation elevates both OH and O_3 under high-NO*x* conditions. The enhanced AOC also intensifies secondary aerosol formation in eastern China, yielding a maximum of 6% increase in $PM_{2.5}$ concentrations during wintertime, driven primarily by accelerated nitrate production. These findings demonstrate that iron-mediated chlorine activation is an important but previously underrepresented driver of global halogen chemistry. Incorporating iron-mediated photochemistry into global models is therefore essential for accurately representing atmospheric oxidation processes and enhancing the reliability of air quality assessments.

1 Introduction

Chlorine chemistry has been recognized as an important factor in regulating atmospheric oxidative capacity (AOC) and air quality. Chlorine radicals (Cl), which react more rapidly with many volatile organic compounds (VOCs) than hydroxyl radical (OH) (Faxon and Allen, 2013; Sun et al., 2025), can alter the abundance and cycling of key atmospheric radicals and oxidants (such as OH, HO_2, RO_2 and O_3) through coupled reaction pathways (Faxon et al., 2015; Chen et al., 2025a; Chen et al., 2025b). Molecular chlorine (Cl_2) is a key chlorine-containing species and can serve as an efficient source of Cl radicals through fast photolysis (Dai et al., 2025; Liu et al., 2017; Priestley et al., 2018). Cl_2 is generally thought to be formed through several pathways, including autocatalytic gas-phase reactions (e.g., ClO + ClO, ClOO + Cl, $ClNO_3$ + Cl), heterogeneous uptake reactions of OH, $ClNO_2$, $ClNO_3$, and HOCl on acidic chloride-containing aerosol, and O_3 uptake by aerosol. Recent laboratory (Wittmer et al., 2015a; Wittmer et al., 2015b; Wittmer and Zetzsch, 2017) and field studies (Chen et al., 2024; Chen et al., 2025b) suggest that aerosols containing soluble iron (Fe) and chloride may generate Cl_2 through Fe(III)-mediated photochemical processes, providing an additional source of Cl radicals. This mechanism has helped explain missing daytime Cl_2 and AOC in regional studies over North China (Chen et al., 2024), the southeastern coast of China (Chen et al., 2025c), and the North Atlantic (Van Herpen et al., 2023). However, most existing work has focused on local environments and the importance of Fe(III)-mediated Cl_2 formation at the global scale remains unclear.

https://doi.org/10.5194/egusphere-2026-1330
Preprint. Discussion started: 18 March 2026

A realistic treatment of soluble Fe aerosols is important for simulating Fe(III)-mediated Cl_2 production. Most simulations about Fe-chlorine chemistry treat aerosol iron solubility with fixed assumptions (e.g., a constant photoreactive Fe fraction of 1.8% (Van Herpen et al., 2023), or prescribed soluble Fe fractions of 4% for dust and 40% for non-dust sources (Chen et al., 2024)). These simplified treatments neglect the dynamic changes in Fe solubility that occur during atmospheric transport, which are driven by aerosol acidification and complexation with organic ligands (Chen and Grassian, 2013). Observations has shown increased Fe solubility from locations near dust sources to downwind regions during atmospheric transport processes (Zhi et al., 2025; Rodríguez et al., 2021; Srinivas et al., 2014; Takahashi et al., 2011). In addition, Fe aerosols from different sources exhibit distinct dissolution behaviors. For example, Fe in coal-combustion particles dissolves much more rapidly than that in mineral dust because of the higher acidity and the presence of reactive organic and inorganic coatings in coal-combustion particles (Baldo et al., 2022). Fe emitted from biomass burning also tend to exhibit higher initial solubility than mineral dust (Wang et al., 2021b; Paris et al., 2010), making its soluble Fe emissions broadly comparable to those from dust sources (Zhang and Zheng, 2024). Therefore, a source-dependent, dynamic and process-based parameterization of Fe solubility is needed to improve the accuracy and reliability of model representations of Fe(III)-mediated Cl_2 photochemical production.

Herein, we updated the chemical mechanism in the GEOS-Chem global atmospheric chemistry model to include Fe(III)-mediated Cl_2 formation pathway together with a more explicit treatment of Fe dissolution. Model performance was evaluated against observations of aerosol Fe concentrations, Fe solubility, and Cl_2 concentrations. The influence of Cl_2 photolysis on the distribution of Cl radicals and other reactive chlorine species, AOC, and the associated feedbacks on air quality were then examined. Our results provide new insights into the role of Fe-driven chlorine chemistry in the atmospheric halogen cycles and highlight the necessity of process-based dynamic Fe solubility for accurately representing iron-halogen interactions in global models.

2 Methods

2.1 Model description

Global chemical transport model GEOS-Chem (version 14.2.3) (https://geoschem.github.io/) was employed to assess the influence of reactive chlorine chemistry on atmospheric processes. The standard chemical mechanism comprises 293 species and 921 reactions, providing a comprehensive representation of the chemical cycling of nitrogen oxides (NO*x*), oxidants (OH, NO_3 and O_3), volatile organic compounds (VOCs), aerosols, and halogens (Cl, Br, and I) in the troposphere and stratosphere. Within the GEOS-Chem standard framework, the formation of Cl_2 is primarily driven by the heterogeneous uptake of HOCl, $ClNO_2$, $ClNO_3$, and OH onto chloride-containing aerosols (e.g. sea salt aerosols). These processes are dynamically modulated by aerosol acidity (pH), liquid water content (LWC), and specific surface area. Although gas-phase reactions (e.g., ClO self-reaction, ClOO + Cl and $ClNO_3$ + Cl) are explicitly represented as well, they contribute marginally to the total Cl_2 budget compared to heterogeneous pathways. The chemical sinks for Cl_2 are photolysis and gas-phase oxidation by OH, with photolysis serving as the dominant sink which generates Cl atoms.

Building on this framework, we integrated a novel Fe(III)-mediated pathway for Cl_2 formation in this study, aiming to quantify the feedback between the iron cycle and reactive chlorine chemistry as well as global AOC.

2.2 Development of the Fe(III)-mediated Cl_2 formation (IMC) mechanism

2.2.1 Emissions of chlorine

In this study, emissions of chlorine from both natural and anthropogenic sources are considered. Natural chlorine emissions are dominated by sea-salt aerosols (SSA), which are calculated based on the spatiotemporal variations in environmental factors, including wind speed, sea surface temperature (SST) and sea-ice fraction. SSA is categorized into fine-mode particles (with diameter of 0.2~1 μm) and coarse-mode particles (with diameter of 1~8 μm), accounting for 16% and 84% of total SSA

https://doi.org/10.5194/egusphere-2026-1330
Preprint. Discussion started: 18 March 2026

emissions, respectively. Correspondingly, sea-salt chloride (pCl) is present at a fixed mass fraction of 55.04% of SSA in each mode (Lewis and Schwartz, 2004). Anthropogenic chlorine emissions (HCl + fine-mode pCl) primarily originate from waste incineration, biomass burning, and industrial processes (Fu et al., 2018; Yin et al., 2022; Chang et al., 2024). Following Fu et al. (2018), a global anthropogenic chlorine emission inventory is constructed and updated to 2023 using the latest activity data and relevant emission factors. The partitioning between HCl and pCl is dynamically determined by the ISORROPIA II thermodynamic equilibrium module (Fountoukis and Nenes, 2007) in GEOS-Chem following Wang et al. (2020).

2.2.2 Emissions of iron

Iron (Fe) emissions include both dust-bound Fe and non-dust Fe. Dust-bound Fe emissions are determined by the corresponding dust emissions and the Fe content of the mineral components. Natural dust emissions are based on a semi-empirical function which combines the topographic source function used in Goddard Chemistry Aerosol Radiation and Transport (GOCART) scheme (Ginoux et al., 2004) with the dust entrainment and deposition (DEAD) mobilization scheme (Zender et al., 2003) by Duncan Fairlie et al. (2007). Anthropogenic dust includes fine particulate matter ($PM_{2.5}$) emissions from anthropogenic fugitive, combustion and industrial processes (AFCID) (Philip et al., 2017). In the model, dust emissions are represented in four distinct size bins with diameters of 0.2~2.0 μm (DST1), 2.0~3.6 μm (DST2), 3.6~6.0 μm (DST3), and 6.0~12.0 μm (DST4). Natural mineral dust is distributed across all four size bins, and originates mainly from the Sahara Desert in North Africa, the Arabian Desert, the deserts of Central and East Asia, and the Australian deserts. In contrast, anthropogenic dust is exclusively assigned to the finest bin (DST1) and primarily concentrated in regions with intensive human activity, including northern China, India, and parts of Europe.

In the standard GEOS-Chem mechanism, dust-bound Fe is simplified by assuming a uniform Fe mass fraction (3.5%) of dust emissions. However, incorporating explicit soil mineralogy is essential for capturing spatial variability and Fe solubility (Gonçalves Ageitos et al., 2023; Nickovic et al., 2012; Scanza et al., 2015; M. S. Johnson and Meskhidze, 2013). In this study, we adopt the soil mineralogical map updated by Nickovic et al. (2012) which is based on the earlier dataset of Claquin et al. (1999). Claquin et al. (1999) identified eight key minerals, including illite (4% as Fe), smectite (11% as Fe), hematite (57.5% as Fe), kaolinite (0.24% as Fe), feldspars (0.34% as Fe), quartz (0% as Fe), calcite (0% as Fe), and gypsum (0% as Fe). Building upon this, Nickovic et al. (2012) introduced a more realistic particle-size distribution by incorporating higher-resolution soil texture data, and redistributed iron oxides across both clay (<2 μm) and silt size, thereby establishing a more physically consistent mineralogical structure. To reduce computational cost while capturing essential chemical processes, only illite, smectite, and hematite are explicitly represented because kaolinite and feldspar collectively accounting for less than 6% of total mineral Fe (as shown in Fig. S1).

Non-dust iron emissions primarily comprise biomass burning (including wildfires) and other anthropogenic sources. Biomass-burning (BB) Fe emissions are scaled from the Quick Fire Emissions Dataset (QFED) since previous studies have demonstrated that QFED offers superior performance in capturing the spatial and temporal variability of fire activities compared to other inventories (Wu et al., 2025). Following the methodology of Hamilton et al. (2019), Fe emissions from BB are parameterized based on a mass ratio to black carbon (Fe:BC = 0.06), with the emitted Fe partitioned into fine and coarse modes at a ratio of 25% and 75%, respectively. Anthropogenic non-BB Fe originates mainly from shipping, aviation, and other human activities. In this study, anthropogenic non-BB Fe emissions are scaled to anthropogenic primary sulfate emissions, assuming a fixed mass ratio of 1:30, following previous studies (Chen et al., 2024; Alexander et al., 2009).

2.2.3 New iron-bearing species

Eight new iron-bearing tracers are introduced into the model. These tracers can be grouped into two major groups based on their source characteristics: dust-bound Fe (Dust Fe) and non-dust Fe (Non-Dust Fe). Dust Fe includes soluble and insoluble fractions of three representative iron-bearing minerals (hematite, illite, and smectite), while non-dust Fe encompasses

https://doi.org/10.5194/egusphere-2026-1330
Preprint. Discussion started: 18 March 2026

contributions from biomass burning and other anthropogenic sources. Since the initial solubility of Fe is strongly influenced by its source and mineralogical structure, differentiated solubility values are assigned to each tracer (as shown in Table 1). In details, dust-bound Fe is initialized with solubilities ranging from 0% to 5%, depending on the chemical stability of the corresponding mineral (Hamilton et al., 2019; Scanza et al., 2018). For biomass-burning Fe, whose reported solubility spans from 2.19% to 46%(Zhang and Zheng, 2024), a representative value of 20% is adopted. For other anthropogenic Fe sources (primarily combustion-derived Fe), a solubility of 4% is applied following previous studies (Luo et al., 2008; Hamilton et al., 2019; Scanza et al., 2018). In addition, each tracer is assigned specific physical proxy properties: dust Fe follows the characteristics of fine-mode dust (DST1), while non-dust Fe uses the hydrophilic and hydrophobic black-carbon properties.

Table 1. Summary of implemented iron-bearing tracers and associated species properties.

Group	Type	Initial solubility	New tracers	Properties proxy
Dust Fe	hematite Fe	0%	hema_sol, hema_insol	DST1
	illite Fe	2.75%	illi_sol, illi_insol	DST1
	smectite Fe	5%	smec_sol, smec_insol	DST1
Non-Dust Fe	biomass burning Fe	20%	anFe_sol, anFe_insol	Black carbon
	other anthropogenic Fe	4%		Black carbon

2.2.4 Parameterization of iron dissolution kinetics

Once released, insoluble Fe undergoes complex chemical processing that facilitates its transformation into soluble forms during atmospheric transport. The conversion is collectively driven by three primary mechanisms: proton-promoted dissolution, ligand-mediated dissolution, and photochemical reductive dissolution. To capture these processes, a multi-stage parameterization scheme is implemented to describe the dynamic dissolution kinetics. Distinct dissolution rates are assigned according to the source of each Fe tracer. Specially, dust-bound Fe generally exhibits chemically stable mineral structures and is treated using the slow kinetics scheme. In contrast, non-dust Fe, characterized by a more amorphous structure and greater specific surface area, follows medium kinetics pathways. The specific dissolution processes and parameterization details are described below, with i denoting the corresponding dissolution regime (slow or medium) in each equation.

Proton-promoted dissolution. Proton-promoted dissolution occurs as acidic species (e.g., H_2SO_4, HNO_3) release H^+ ions that attack the crystal lattice of iron oxides, mobilizing iron into the aerosol phase. This process is supported by numerous field observations which demonstrate a significant positive correlation between iron solubility and acidic ions (Zhang et al., 2021; Zhang et al., 2023; Zhu et al., 2020). Following Meskhidze et al. (2005), the acid-promoted dissolution rate constant, $k(Fe_{sol})_{proton}$, is parameterized as Eq (1):

$$k(Fe_{sol})_{proton} = K_i(T) \times \alpha(H^+)^{m_i} \times f(\nabla G_r) \times A_i \times MW \quad \text{Eq(1)}$$

where $K_i(T)$ (mol m^{-2} s^{-1}) is the temperature-dependent rate constant, m_i (unitless) is the empirical reaction order and A_i (m^2 g^{-1}) is the specific surface area of the particle, with distinct formulations or values adopted for slow and medium dissolution regimes following Hamilton et al. (2019). $f(\nabla G_r)$ is the thermodynamic response function, which accounts for the system's deviation from chemical equilibrium. Based on Luo et al. (2008), this value is simplified to 1. MW is the molecular weight of the species with unit of g mol^{-1}. $\alpha(H^+)$ represents the proton activity, which can be calculated as Eq(2):

$$\alpha(H^+) = 10^{-pH} \quad \text{Eq(2)}$$

Ligand-mediated dissolution. Ligand-mediated dissolution involves the formation of stable complexes between organic ligands (e.g., dicarboxylic acids, oxalate) and dissolved Fe(III), which effectively inhibits the hydrolysis and subsequent precipitation of iron thus increasing its solubility. Extensive studies have highlighted that organic ligands significantly enhance iron solubility and bioavailability, particularly in organic-rich environments. As oxalate is the most abundant dicarboxylic acid in the atmosphere, field observations have consistently identified a strong positive correlation between oxalate concentrations and soluble iron(Li et al., 2024; Zhang et al., 2021; Zhang et al., 2024). Consequently, this study adopts a ligand-enhanced dissolution parameterization following Hamilton et al. (2019), with the reaction rate expressed as:

https://doi.org/10.5194/egusphere-2026-1330
Preprint. Discussion started: 18 March 2026

$$k(Fe_{sol})_{ligand} = a_i \times [C_2O_4^{2-}] + b_i \quad \text{Eq(3)}$$

where a_i and b_i represent the source-specific rate coefficients, consistent with the values in Hamilton et al. (2019).

Since explicitly resolving full photochemical formation mechanism of oxalate would impose substantial computational cost, oxalate concentrations are diagnosed using a proxy approach. Following Scanza et al. (2018), secondary organic aerosol (SOA) is adopted as the proxy, as its formation pathways are closely associated with the photochemical oxidation of organic precursors that also lead to oxalate production. Finally, concentration of oxalate ($[C_2O_4^{2-}]$(μmol L^{-1})) is calculated from simulated SOA concentrations as Eq (4):

$$[C_2O_4^{2-}] = 15 \times \frac{[SOA]}{Max[SOA]} \quad \text{Eq(4)}$$

The scaling factor of 15 is adopted from multi-model sensitivity test, which has been shown to reasonably capture the spatial characteristics of global oxalate distributions (Scanza et al., 2018).

Photochemical reductive dissolution. Photochemical reductive dissolution involves the reduction of Fe(III) to the more soluble Fe(II) via ligand-to-metal charge transfer (LMCT) activated by solar radiation absorbing. However, since redox cycling equilibrates much faster than aerosol transport, no additional valence-specific tracers are introduced. Instead, the instantaneous Fe(III)/Fe(II) ratio is diagnosed under a quasi-steady-state assumption during the calculation of Cl_2 production (Section 2.2.5), determined by the local photochemical radiation flux.

2.2.5 Parameterization of IMC mechanism

In this study, the total dissolved iron ($totFe_{sol}$, unit: mol m^{-3}) is defined as the sum of soluble Fe originating from both mineral dust and non-dust (anthropogenic and biomass burning) sources:

$$totFe_{sol} = hema_{sol} + illi_{sol} + smec_{sol} + anFe_{sol} \quad \text{Eq(5)}$$

where $hema_{sol}$, $illi_{sol}$, $smec_{sol}$ represent soluble iron from hematite, illite, and smectite, respectively, and $anFe_{sol}$ denotes soluble Fe from biomass burning and other anthropogenic emissions.

Since the formation of Cl_2 depends strongly on the solar-radiation-driven Fe redox cycle, the fraction of Fe(II) is diagnosed following the empirical formulation of Van Herpen et al. (2023) as Eq(6):

$$f(FeII) = k_2 \times \left[\frac{I}{I_0} \times \left(k_1 + k_2 \times \frac{I}{I_0}\right)\right]^{-1} \quad \text{Eq(6)}$$

where I is the instantaneous solar irradiance (W m^{-2}) and I_0 is the reference irradiance (600 W m^{-2}). The rate constants k_1(0.19 min^{-1}) and k_2(1.9 min^{-1}), representing the oxidation rate of Fe(II) to Fe(III) and photoreduction rate of Fe(III) to Fe(II), respectively, following the values specified in Van Herpen et al. (2023).

Laboratory studies have shown that IMC mechanism can be suppressed under specific chemical conditions. Specifically, when the molar ratio of Cl^-/Fe(III) reaches approximately 955, the formation of photosensitive iron-chloride complexes is substantially inhibited due to the extremely low concentration of total Fe(III), leading to negligible Cl_2 production (Wittmer et al., 2015b). To avoid overestimating the contribution of this pathway in "high-chloride, low-iron" environments, this critical threshold is incorporated into the parameterization. Consequently, the final expression for the Cl_2 production rate (P_{Cl_2}, mol m^{-3} min^{-1}) is as Eq(7):

$$P_{Cl_2} = totFe_{sol} \times k_1 \times f(FeII) \times \frac{1}{2} \quad \left(for\ \frac{[Cl^-]}{[Fe(III)]} < 955\right) \quad \text{Eq(7)}$$

2.3 Model simulation scenarios

To evaluate the atmospheric impacts of IMC mechanism, we conduct three sensitivity simulations. The three scenarios differ in their treatment of Cl_2 formation and iron solubility (Table 2). The "Base" simulation excludes both the IMC mechanism and iron solubility effects. The "FixFeS" simulation includes the IMC mechanism with a uniform iron solubility of 1.8 % as Van

https://doi.org/10.5194/egusphere-2026-1330
Preprint. Discussion started: 18 March 2026

Herpen et al. (2023). The "VarFeS" simulation incorporates both the IMC mechanism and a dynamic representation of iron solubility modulated by proton processing, organic complexation, and mineralogical variability. This configuration enables us to separately evaluate the impact of the IMC mechanism and the role of iron solubility on Cl_2 formation.

Table 2. Summary of sensitivity scenarios.

Experiment (Scenario)	IMC mechanism	Iron solubility treatment
Exp1(Base)	No	Not included
Exp2(FixFeS)	Yes	Fixed at 1.8%
Exp3(VarFeS)	Yes	Process-based variable solubility

Each simulation is performed at 4° latitude × 5° longitude horizontal resolution with 47 vertical levels (extending from the surface to 0.01 hpa), driven by MERRA-2 meteorological fields. All runs are initialized from identical concentration fields representative of realistic atmospheric conditions and span a 1.5-year period from 1 June 2022 to 31 December 2023. The first six months serves as a spin-up to minimize the influence of initialization, and all analyses are based on output from the year of 2023. Aside from the updated chlorine and iron emissions described above (section 2.2.1 and 2.2.2), the simulations use the standard suite of GEOS-Chem emission inventories. In details, anthropogenic and ship emissions of CO, NO*x*, NH_3, SO_2, VOCs, BC and OC are taken from the Community Emissions Data System (CEDS) version 2 (Hoesly et al., 2018). Biomass burning emissions follow QFED version 2.5r1 (Darmenov and Da Silva, 2015) while biogenic VOC emissions are calculated online by Model of Emissions of Gases and Aerosols from Nature (MEGAN) version 2.1 (Guenther et al., 2012), as implemented by Hu et al. (2015). Aircraft emissions of CO, NO*x*, SO_2, VOCs, BC and OC are taken from AEIC (Stettler et al., 2011).

2.4 Observations for model evaluation

To assess model performance for iron dissolution processes and IMC mechanism, simulation results are evaluated against compiled observational datasets of solubility of iron and concentration of iron as well as Cl_2. Global datasets provided by Myriokefalitakis et al. (2018) and Mahowald et al. (2009) are expanded with additional new observations records for both Fe concentration and solubility (as shown in Table S1). These additional data points primarily cover Asian regions, which are sparsely represented in previous datasets but are characterized by high pCl emissions. In total, the final synthesized dataset comprises 1399 and 1089 observational points for total Fe concentration and Fe solubility, respectively.

In contrast to iron, observational data for Cl_2 are far more limited. Reported Cl_2 concentrations range from a few ppt to approximately 1 ppb, indicating a wide dynamic range driven by regional emission characteristics and rapid atmospheric reactions. Currently available Cl_2 observations are characterized by limited spatial coverage, predominantly distributed across the coastal regions of China, North America, Europe, and Canada (as shown in Fig. S2). For this study, a total of 25 observational points of Cl_2 are compiled. Since several sites report only peak values or nighttime averages, measurements are subsequently normalized for comparison with the model results. Detailed information for the observational dataset of Cl_2 is provided in Table S2.

3 Results and discussions

3.1 Model evaluation

3.1.1 Evaluation of total Fe concentrations and solubility against observations

Since three simulation scenarios share identical total iron emissions and transport processes, they yield effectively the same total aerosol Fe concentrations. Moreover, while the "Base" and "FixFeS" scenarios employ either no or uniform iron solubility, only the "VarFeS" scenario incorporates a physically based, dynamic representation of iron solubility. Therefore, the comparison of total Fe concentrations and solubility with observations in this section focuses on simulation results from the

https://doi.org/10.5194/egusphere-2026-1330
Preprint. Discussion started: 18 March 2026

"VarFeS" scenario.

As illustrated in Fig. 1, global distribution of total aerosol Fe concentration is broadly consistent between the model simulations and the available observations. Elevated Fe concentrations (typically exceeding 2 μg m^{-3}) are concentrated over major arid and semi-arid regions, including the North Africa, the Middle East and Central Asia, reflecting the dominance of intense mineral dust emissions in these areas (Wu et al., 2021; Shao et al., 2011). Similarly, enhanced Fe loadings are also simulated in regions characterized by extensive anthropogenic activities, such as the North China Plain, Indian and Europe. In contrast, over remote oceanic regions far from dust sources and in areas with limited anthropogenic (like central Pacific and Southern Ocean), both simulations and observations exhibit low Fe loadings, consistent with progressive deposition during long-range transport. In addition, the model also effectively captures the primary intercontinental transport pathways, such as atmospheric outflow of North African dust toward North Atlantic and South America, and the transport of Central Asian dust to the North Pacific (Zan et al., 2025), as evidenced by the gradually decreasing Fe concentration along these routes.

The comparison between simulated and observed Fe solubility reveals more pronounced regional heterogeneity, reflecting the combined effects of iron speciation, source characteristics, and atmospheric processing. Modelled surface mean value of total Fe solubility at all the observational sites globally is 3.4%, which is in good agreement with the observational value of 3.2%. Generally, the model simulates low solubility (typically < 2%) over major dust source regions such as the Sahara Desert, the Gobi Desert, and inland Australia Desert, consistent with the dominance of poorly soluble iron oxides in freshly emitted mineral dust in these areas. In contrast, remote oceanic regions exhibit substantially higher solubility, in line with previous observational evidences that Fe solubility increases during long-range transport (Takahashi et al., 2011; Srinivas et al., 2014; Rodríguez et al., 2021). Notably, the observational datasets display substantial inherent spatial variability, with solubility values differing by orders of magnitude even between nearby sites. This strong spatial heterogeneity highlights the sensitivity of Fe solubility to local environmental conditions, including acidic gases concentrations, organic ligands availability, the diversity of aerosol origins, and even sample storage and analytical protocols. Overall, the model reproduces the large-scale gradients in Fe solubility, but local discrepancies persist, underscoring the regional diversity of solubilization mechanisms and the remaining uncertainties in their parameterization within the model.

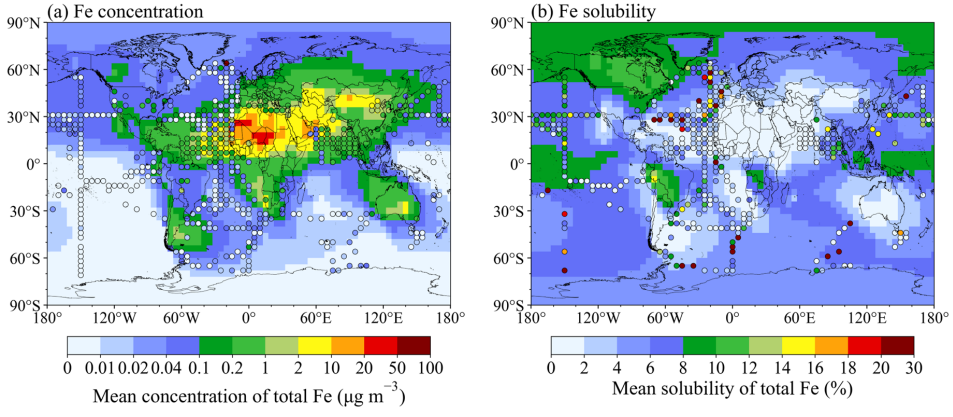

Figure 1. Comparison of modelled annual mean surface results with observational records for total aerosol Fe concentration (a) and Fe solubility (b). Observations (circles) have been averaged to the resolution of the model grid.

3.1.2 Evaluation of Cl_2 concentrations against observations

Incorporating alternative dissolution pathways and IMC mechanism markedly improves the model's ability to reproduce observed Cl_2, with the correlation coefficient increasing from 0.55 ("Base") to 0.88 ("VarFeS") and reducing the normalized mean bias (NMB) from –82.5% to 45.9%. Specifically, for lower Cl_2 concentrations (below 10 pptv), the improvement is even more pronounced, with the NMB shifting from –86.3% to 18.0%. As shown in Fig. 2, the absence of IMC mechanism in the

https://doi.org/10.5194/egusphere-2026-1330
Preprint. Discussion started: 18 March 2026

"Base" scenario leads to a systematic underestimation of Cl_2, with simulated concentrations up to 83 % lower than observations. In the "FixFeS" scenario, a fixed 1.8 % fraction of photoactive Fe enhances model performance but still yields Cl_2 levels at only ~30 % of the observations. This bias reflects the inability of a constant fraction to represent realistic photoactive Fe abundances in regions strongly influenced by anthropogenic emissions such as the North Atlantic, where the mean value of photoactive Fe reaches 32 % due to pollutants from North America and Europe (Chen and Siefert, 2004). In contrast, by incorporating source-dependent variable Fe dissolution mechanism, the Cl_2 concentrations in the "VarFeS" scenario match observations better across most sites, even though an overall overestimation exists. This overestimation may result from the inherent limitations of the IMC parameterization. Since the rate constants k_1 and k_2 adopted in this study are derived from field measurements conducted in the North Atlantic (Van Herpen et al., 2023), so extending these regional constrained empirical parameters to a global scale may introduce inherent uncertainties, as the chemical composition and aging of aerosols vary geographically. In addition, the current IMC parameterization also implicitly assumes a 100% conversion efficiency, where every two Fe(III)/Fe(II) photoactivate cycle yield one Cl_2 molecule production (as reflected in the stoichiometric factor). However, photo-induced electrons or intermediate species (e.g., Cl radicals) may undergo competitive quenching or side reactions with other reducing constituents such as organic matter or reduced sulfur species. Thus, actual Cl_2 yield may be overestimated under certain environmental conditions.

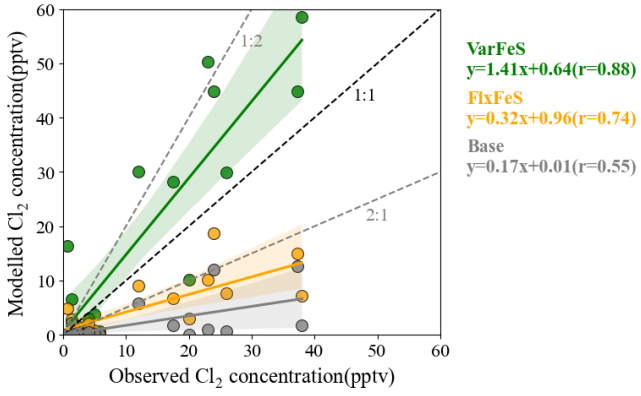

Figure 2. Comparison of modelled and normalized observed Cl_2 concentrations under different scenarios.

3.2 Effects on reactive chlorine species

Cl_2

As illustrated in Fig. 3, the inclusion of the IMC mechanism induces a profound shift in global mean Cl_2 concentrations, which increases from 0.4 (with a range of 0-11) pptv in the "Base" scenario to 2.2 (with a range of 0.01-57) pptv in the "VarFeS" scenario. In the "Base" case, elevated concentrations of Cl_2 are confined mainly to coastal China, driven by heterogeneous uptake of $ClNO_2$ onto the surface of particulate chloride. In the "VarFeS" scenario for 2023, however, pronounced regional and seasonal heterogeneities exist in global Cl_2 distribution. Prominent Cl_2 hotpots are identified in the western Canada (WC: 8.2 ± 5.5 pptv), the eastern China (EC: 24.9 ± 16.3 pptv), the southern Asia (SA: 10.2 ± 7.6 pptv), the northern Eurasia (NE: 5.5 ± 2.3 pptv), and the tropical Atlantic (TA: 4.9 ± 1.8 pptv) (see Fig. S3 for regional definitions). Furthermore, distinct seasonal patterns are observed in these regions (Fig. S4). In WC, the Cl_2 enhancement is predominantly triggered by extreme wildfire events in 2023 in summer. Wildfires simultaneously release large amounts of Fe and pCl aerosols from biomass burning within a short period (Tang et al., 2021; Zhang et al., 2022), thereby eliminating precursor limitations on Cl_2 formation processes. During summer, when solar radiation is stronger, the concentration of Cl_2 reaches 11.4 ± 10.3 pptv, which is 2.4 times higher than it in winter in Canada. By contrast, Cl_2 enhancements in EC (mainly in North China Plain, NCP) and SA (mainly in India) are significantly amplified during winter. In winter, elevated anthropogenic and dust-derived Fe from heating-

https://doi.org/10.5194/egusphere-2026-1330
Preprint. Discussion started: 18 March 2026

related activities (coal and biomass combustion) and enhanced dust resuspension, together with high pCl emissions from coal burning and biomass burning, strongly favor Cl_2 production. Meanwhile, the meteorology during winter including shallow planetary boundary layer heights, frequent stagnant conditions, and weakened solar radiation further suppresses vertical dispersion and photolysis of Cl_2. This extends the chemical lifetime of Cl_2, facilitating its persistent accumulation in the surface layer. Consequently, the NCP and the northern India exhibit the strongest Cl_2 enhancement during winter, with mixing ratios reaching 40~60 pptv in December. Similarly, meteorological conditions and remarkable anthropogenic dust Fe emissions lead to noticeable Cl_2 production in NE during wintertime as well. In contrast to these regions, Cl_2 maxima over the TA are governed by the long-term background input of natural mineral dust Fe. Although dust-bound Fe possesses lower solubility, the massive total flux ensures that soluble Fe concentrations (43.5 ± 19.0 ng m^{-3}), far above the global mean (7.1 ± 14.8 ng m^{-3}), coupled with abundant sea-salt chloride emissions, maintains a stable Cl_2 background in TA.

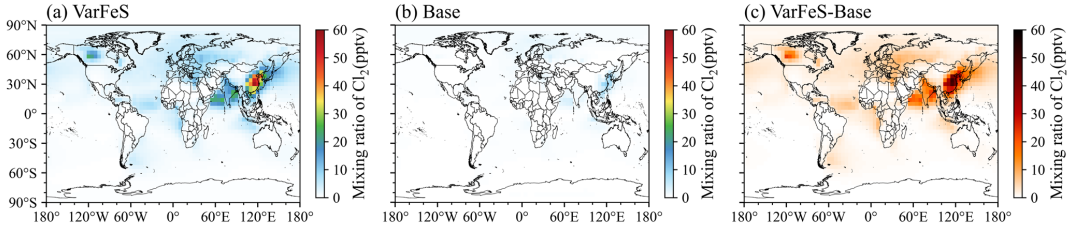

Figure 3. Spatial distributions of global surface Cl_2 mixing ratios under different simulation scenarios (a, b) and their corresponding absolute differences (c).

Other reactive chlorine species

Changes in Cl_2 concentrations exert substantial downstream impacts on the broader reactive chlorine species, as depicted in Fig. 4. The spatial distribution of elevated Cl radicals (Fig. 4a) closely tracks Cl_2 hotspots, reflecting the rapid photolysis of Cl_2. This efficient conversion of Cl_2 to Cl enlarges atmospheric Cl radical reservoir within these source regions and extends its influence into downwind environments, yielding a maximum Cl radical increase of 2.14×10^4 atoms cm^{-3} compared to the "Base" scenario. The amplified Cl radical pool further intensifies the cycle involving Cl, O_3, and ClO (ClO*x* cycling), driving a global rise in ClO concentrations by an average factor of 3.5, with peak enhancements reaching 84-fold (Fig. 4b). Strengthened ClO*x* cycling subsequently deepens its interaction with HO*x* and NO*x* chemical families, where rising ClO levels drive a 2.6-fold average increase in HOCl via the ClO and HO_2 reaction (Fig. 4c). This modelled response aligns closely with recent field observations which indicated that photochemical processing of aerosol iron is a key driver of daytime Cl_2 production and the subsequent formation of HOCl (Chen et al., 2025c).

Beyond the major Cl_2 production hotspots over Canada, northern China and India, the Tibetan Plateau (TP) also exhibits pronounced changes in Cl, ClO, and HOCl, likely driven by long-range transport from Southern Asia. Previous studies have shown that pre-monsoon biomass-burning emissions from western India can contribute over 60% of $PM_{2.5}$ concentrations on the TP via westerly transport (Yang et al., 2022). Besides, mineral dust from the Thar Desert(Wang et al., 2021a) and anthropogenic pollution from the Indo-Gangetic Plain (Xia et al., 2011) can be transported to the Himalayas by the combined effects of the "Himalayan pump" and the prevailing pre-monsoon circulation. Thus, it is plausible that biomass-burning aerosols enriched in pCl and Fe, together with Fe-bearing mineral dust, facilitate the production of Cl_2. Then, under the TP's intense ultraviolet radiation, Cl_2 is rapidly photolyzed, ultimately driving the pronounced enhancements in other reactive chlorine species observed in this region.

https://doi.org/10.5194/egusphere-2026-1330
Preprint. Discussion started: 18 March 2026

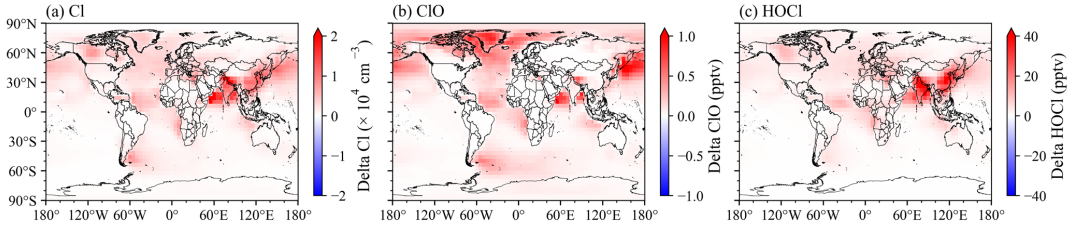

330 **Figure 4.** Corresponding absolute differences between the "VarFeS" and "Base" simulations for different reactive chlorine species.

3.3 Effects on atmospheric oxidative capacity (AOC)

RO_2

Inclusion of the IMC mechanism in "VarFeS" scenario significantly alters the concentration of RO_2, with global annual mean
335 RO_2 concentration increasing by approximately 0.1 pptv and peak enhancement reaching 2 pptv. The spatial distribution of RO_2 enhancement closely follows the major Cl_2 hotspots which are driven by the role of Cl radicals. Since reaction rate constants for Cl radicals with most typical VOCs (such as methane, ethane, isoprene and α-pinene) exceed those for OH radicals by 1~2 orders of magnitude (Faxon and Allen, 2013; Sun et al., 2025), the Fe(III)-mediated Cl source greatly accelerates the production of R radicals, thereby driving rapid increases in RO_2. As a result, RO_2 increases by up to 30% (2.3%
340 on global average), with the largest enhancements occurring in open biomass burning regions across the mid-to-high latitudes of the Northern Hemisphere. These results indicate that in regions with abundant VOC precursors (e.g., intense wildfire emissions), the contribution of Cl radicals generated via IMC mechanism can be strongly amplified. Besides, despite extremely low background pollutant levels, the relative enhancement of RO_2 remains high over Antarctica. This can be attributed to long-range transport of iron-containing aerosols from South American wildfires to the Southern Ocean, where Fe(III)-mediated
345 photochemistry makes Cl radicals a major oxidant in these areas. Given the very low baseline RO_2 concentrations, even a slight increase leads to a disproportionately large relative change.

OH and HO_2

On a global scale, the spatial distribution of surface OH and HO_2 exhibit substantial changes driven primarily by chlorine-initiated cycling. With the inclusion of IMC mechanism, the global annual mean surface OH concentrations decreased
350 by 2×10^4 atoms cm^{-3}, which corresponds to a 5.7% relative reduction compared to the "Base" scenario. This decline is particularly evident in NO*x*-limited oceanic and remote regions, driven by two synergistic pathways: first, Cl-initiated chemistry may suppress HO*x* recycling as conversion of HO_2 and OH to Cl/ClO leads to a synchronized decline in OH levels(Simpson et al., 2015; Chen et al., 2024); secondly, since O_3 photolysis represents the primary source of OH radicals in most environments(Lelieveld et al., 2016), the widespread reduction of O_3 abundances by Cl radicals in these regions further
355 curtails OH production. However, the variation characteristics are different regionally depending on the HO*x* recycling efficiency. The oxidation of VOCs by Cl radicals generates additional RO_2, which subsequently enhances HO_2 production (Dai et al., 2025). In NO*x*-rich regions, elevated NO levels substantially accelerate the conversion of HO_2 to OH, thereby strengthening HO*x* recycling and increasing OH abundances. The effect is particularly pronounced over the NCP, where enhanced RO_2 formation and efficient HO_2-to-OH conversion lead to a localized OH increase of up to 14%. Similarly, parts
360 of the United States and Europe show rising OH concentrations, as strengthened HO*x* cycling in these regions effectively boosts OH levels. In contrast, although a substantial rise in HO_2 is also predicted for India, the resulting change in OH remains minimal. This suggests that relatively abundant VOCs in India (Pakkattil and Ghude, 2025) already drive HO*x* recycling toward high efficiency and near-saturation. Consequently, further regeneration becomes primarily constrained by the limited availability of NO*x*, thus making OH production less sensitive to additional chlorine-driven HO_2 inputs.

https://doi.org/10.5194/egusphere-2026-1330
Preprint. Discussion started: 18 March 2026

O_3

As depicted in Fig. 5, O_3 shows two distinct responses due to regional variations in photochemical sensitivity to NO*x*. Across most global regions with low NO*x* levels, the concentration of O_3 declines as elevated Cl radicals tend to accelerate O_3 loss through direct reaction (forming ClO). Conversely, the North China Plain (NCP) stands out as one of the few regions worldwide where O_3 increases markedly, which is attributed to its photochemical environment dominated by high NO*x* levels and strong "VOCs limitation regime" (Hao et al., 2024; Yao et al., 2024; Liu et al., 2025). Under NO*x*-excess conditions, the acceleration of VOCs oxidation by Cl radicals substantially increases RO_2 concentrations and thereby promotes photochemical O_3 production. Furthermore, while India experiences comparable NO*x* levels and elevated Cl_2 concentrations to those in NCP, a slight decrease in O_3 concentration is observed due to its distinct O_3 photochemical regime. Recent satellite evidence confirms that the majority of India predominantly resides within a "NO*x* limited regime" with respect to ozone formation (Pakkattil and Ghude, 2025; Rawat and Naja, 2022). Consequently, the combination of chlorine-driven NO*x* depletion together with the direct consumption of O_3 by Cl leads to decreased O_3 levels over India.

Overall, incorporating the IMC mechanism exerts regionally differentiated impacts on the global AOC. Over the NCP, atmospheric AOC is markedly enhanced, driven by accelerated radical chain reactions and elevated oxidant levels. In other regions, however, the influence of Cl chemistry is jointly modulated by the local photochemical environment, the NO*x*-VOCs sensitivity regime, and background oxidant levels, resulting in a complex pattern in which enhancements and suppressions coexist.

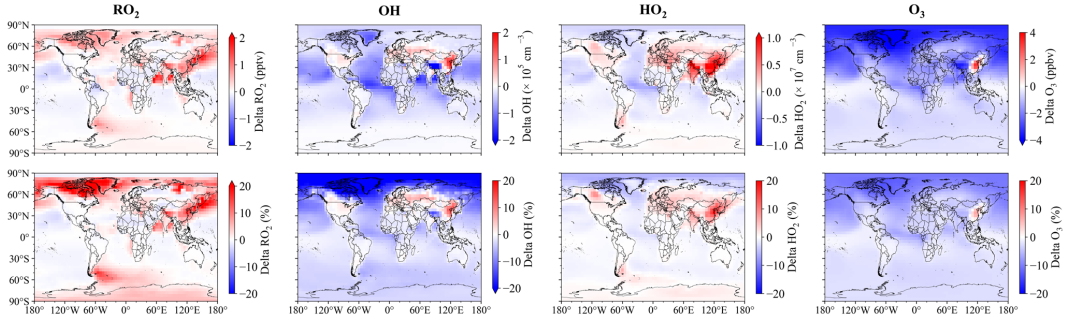

Figure 5. Comparison of absolute changes (top panel: VarFeS-Base) and relative changes (bottom panel: (VarFeS-Base)/Base) in annual mean surface concentration of RO_2, OH, HO_2 and O_3.

3.4 Effects on fine particle matters

As shown in Fig. 6, chlorine chemistry activation by the IMC mechanism acts as an indirect driver of fine particulate matter ($PM_{2.5}$) pollution, particularly across the mid-to-high latitude land areas of the Northern Hemisphere. While slight increases of roughly 0.5% are found in western Europe, northern America, Canada, and parts of the Arctic Ocean, the most pronounced response appears over the NCP, where $PM_{2.5}$ rises by up to 2.5% (+2.2 μg m^{-3}). In the NCP, the $PM_{2.5}$ enhancement is predominantly driven by nitrate formation (+1.9 μg m^{-3}) (Fig. S5). This nitrate-dominated response is closely linked to elevated Cl_2 concentrations. Photolysis of Cl_2 generates highly reactive Cl radicals that substantially increase OH levels over the NCP. Since OH radicals are the critical daytime oxidants driving the conversion of nitrogen oxides into nitrate, the strengthened oxidizing environment accelerates nitrate formation and thereby increases $PM_{2.5}$ mass concentration. Furthermore, under stagnant meteorology and high precursor emissions in the wintertime, this effect becomes significantly amplified with maximum $PM_{2.5}$ increases over the NCP reaching 6% (Fig. S6). It should be noted, however, that the model employs a simplified SOA scheme, which likely leads to an underestimation of the impact of chlorine chemistry on SOA formation and, consequently, on total $PM_{2.5}$ concentrations. Therefore, future regional air-quality management strategies need to consider the roles of iron cycling and halogen chemistry jointly.

https://doi.org/10.5194/egusphere-2026-1330
Preprint. Discussion started: 18 March 2026

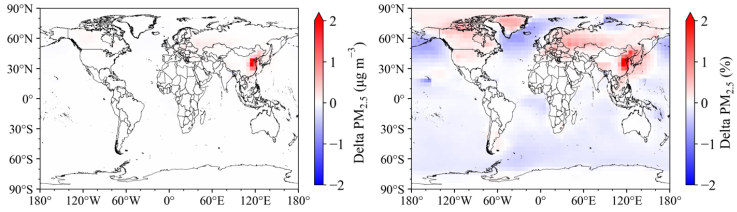

Figure 6. Comparison of absolute changes (left: VarFeS-Base) and relative changes (right: (VarFeS-Base)/Base) in annual mean surface concentration of $PM_{2.5}$.

4 Conclusions

We updated the GEOS-Chem global atmospheric chemistry model to include a mechanistic representation of Fe(III)-mediated Cl_2 production pathway, accounting for the dynamic solubility of iron driven by acid processing, organic complexation, and mineralogical variability. This update improves the model's ability to reproduce Cl_2 concentrations, increasing the correlation coefficient from 0.55 to 0.88 relative to "Base" scenario.

Substantial changes in global reactive chlorine species and atmospheric oxidative capacity emerge following the model update. Global mean tropospheric Cl_2 increases from 0.4 to 2.2 pptv, with hotspots exceeding 40 pptv over the eastern China and India. Rapid photolysis of Cl_2 expands the Cl radical reservoir and strengthens VOCs oxidation, leading to a 2.3 % increase in global RO_2 (peaking at 30 % in wildfire-influenced regions). Enhanced Cl-driven oxidation perturbs HO*x* recycling by O_3 depletion and converting OH and HO_2 into Cl and ClO in the remote marine regions, leading to a synchronized decline in OH and ultimately a 5.7% reduction in the global mean OH levels. In contrast, the eastern China exhibits concurrent increases in both O_3 and OH (up to +14 %), as Cl-accelerated VOCs oxidation under its strongly VOC-limited chemical regime. Such perturbations significantly impact regional air quality. Specifically, Fe-Cl chemistry elevates $PM_{2.5}$ mass concentrations across the mid-to-high latitude Northern Hemisphere. The most pronounced response occurs in eastern China, where $PM_{2.5}$ increases by up to 2.5 %, primarily driven by accelerated NO*x* oxidation under elevated daytime OH. This effect is further intensified during stagnant winter episodes, with localized $PM_{2.5}$ surges reaching 6 %.

In summary, our updated mechanism offers a mechanistically consistent framework for representing the interactions among mineral-dust iron, anthropogenic iron, and halogen chemistry. Model results demonstrate that Fe(III)-mediated Cl_2 production pathway exerts a meaningful influence on global radical chemistry and $PM_{2.5}$ loadings, which underscores the importance of accounting for iron-halogen coupling chemistry in future air-quality assessments and mitigation strategies.

Data availability

Data will be made available on request.

Author contributions

JC: conceptualization, methodology, formal analysis, software, visualization, writing (original draft preparation), writing (review and editing). XS: methodology. CQ: methodology. JL: methodology. QC: methodology, funding acquisition, writing (review and editing). XF: conceptualization, methodology, resources, funding acquisition, supervision, writing (review and editing).

https://doi.org/10.5194/egusphere-2026-1330
Preprint. Discussion started: 18 March 2026

Competing interests

The authors declare that they have no conflict of interest.

Acknowledgements

We would like to thank Prof. Nicholas Meskhidze and Prof. Douglas Hamilton from NC State University for their help on Fe parameterization.

Financial support

This research was supported by Natural Science Foundation of Guangdong Province (2025A1515012215), Municipal Science and Technology Innovation Commission of Shenzhen (JCYJ20220530143007016), the National Key R&D Program of China (2023YFC3709204) and Guangdong Talent Program (2023QN10L113), QC acknowledges Hong Kong Research Grants Council (Grant No. 15219722, 25231725, and 15223221).

References

Alexander, B., Park, R. J., Jacob, D. J., and Gong, S.: Transition metal-catalyzed oxidation of atmospheric sulfur: Global implications for the sulfur budget, J Geophys Res-Atmos, 114, D02309,doi: https://doi.org/10.1029/2008JD010486, 2009.

Baldo, C., Ito, A., Krom, M. D., Li, W. J., Jones, T., Drake, N., Ignatyev, K., Davidson, N., and Shi, Z. B.: Iron from coal combustion particles dissolves much faster than mineral dust under simulated atmospheric acidic conditions, Atmos. Chem. Phys., 22, 6045-6066,doi: 10.5194/acp-22-6045-2022, 2022.

Chang, D., Li, Q., Wang, Z., Dai, J., Fu, X., Guo, J., Zhu, L., Pu, D., Cuevas, C. A., Fernandez, R. P., Wang, W., Ge, M., Fung, J. C. H., Lau, A. K. H., Granier, C., Brasseur, G., Pozzer, A., Saiz-Lopez, A., Song, Y., and Wang, T.: Significant chlorine emissions from biomass burning affect the long-term atmospheric chemistry in Asia, Natl. Sci. Rev., 11, nwae285,doi: 10.1093/nsr/nwae285, 2024.

Chen, G., Chen, Z., Zhang, Y., Fan, X., Xu, L., Lin, Z., Ji, X., and Chen, J.: Enhanced oxidation capacity driven by pollution-induced chlorine chemistry in the coastal atmosphere, npj Clim. Atmos. Sci., 8,doi: 10.1038/s41612-025-01133-6, 2025a.

Chen, G. J., Fan, X. L., Lin, Z. Y., Ji, X. T., Chen, Z. Y., Xu, L. L., and Chen, J. S.: Driving factors and photochemical impacts of Cl_2 in coastal atmosphere of Southeast China, npj Clim. Atmos. Sci., 8, 2397-3722,doi: 10.1038/s41612-025-01022-y, 2025b.

Chen, G. J., Fan, X. L., Yu, S. C., Tham, Y. J., Lin, Z. Y., Ji, X. T., Xu, L. L., and Chen, J. S.: HOCl formation driven by photochemical processes enhanced atmospheric oxidation capacity in a coastal atmosphere, Environ. Sci. Technol., 59, 5164-5171,doi: 10.1021/acs.est.5c01363, 2025c.

Chen, H. and Grassian, V.: Iron dissolution of dust source materials during simulated acidic processing: the effect of sulfuric, acetic, and oxalic acids., Environ. Sci. Technol., 47 18, 10312-10321,doi: 10.1021/es401285s, 2013.

Chen, Q., Wang, X., Fu, X., Li, X., Alexander, B., Peng, X., Wang, W., Xia, M., Tan, Y., Gao, J., Chen, J., Mu, Y., Liu, P., and Wang, T.: Impact of molecular chlorine production from aerosol iron photochemistry on atmospheric oxidative capacity in North China, Environ. Sci. Technol., 58, 12585-12597,doi: 10.1021/acs.est.4c02534, 2024.

Chen, Y. and Siefert, R. L.: Seasonal and spatial distributions and dry deposition fluxes of atmospheric total and labile iron over the tropical and subtropical North Atlantic Ocean, J Geophys Res-Atmos, 109, D09305,doi: 10.1029/2003jd003958, 2004.

Claquin, T., Schulz, M., and Balkanski, Y. J.: Modeling the mineralogy of atmospheric dust sources, J Geophys Res-Atmos, 104, 22243-22256,doi: 10.1029/1999jd900416, 1999.

Dai, J. N., Wang, T., Shen, H. Q., Xia, M., Sun, W. H., and Brasseur, G. P.: Significant impact of a daytime halogen oxidant

https://doi.org/10.5194/egusphere-2026-1330
Preprint. Discussion started: 18 March 2026

on coastal air quality, Environ. Sci. Technol., 59, 2169-2180,doi: 10.1021/acs.est.4c08360, 2025.

Darmenov, A. and da Silva, A. M.: The Quick Fire Emissions Dataset (QFED)-Documentation of versions 2.1, 2.2 and 2.4, NASA38, NASA/TM-2015-104606, 2015.

Duncan Fairlie, T., Jacob, D. J., and Park, R. J.: The impact of transpacific transport of mineral dust in the United States, Atmos. Environ., 41, 1251-1266,doi: 10.1016/j.atmosenv.2006.09.048, 2007.

Faxon, C., Bean, J., and Ruiz, L.: Inland concentrations of Cl_2 and $ClNO_2$ in southeast Texas suggest chlorine chemistry significantly contributes to atmospheric reactivity, Atmosphere, 6, 1487-1506,doi: 10.3390/atmos6101487, 2015.

Faxon, C. B. and Allen, D. T.: Chlorine chemistry in urban atmospheres: a review, Environ. Chem., 10, 221-233,doi: 10.1071/en13026, 2013.

Fountoukis, C. and Nenes, A.: ISORROPIA II: a computationally efficient thermodynamic equilibrium model for K^+-Ca^{2+}-Mg^{2+}-NH_4^+-Na^+-SO_4^{2-}-NO_3^--Cl^--H_2O aerosols, Atmos. Chem. Phys., 7, 4639-4659,doi: 10.5194/acp-7-4639-2007, 2007.

Fu, X., Wang, T., Wang, S., Zhang, L., Cai, S., Xing, J., and Hao, J.: Anthropogenic emissions of hydrogen chloride and fine particulate chloride in china, Environ. Sci. Technol., 52, 1644-1654,doi: 10.1021/acs.est.7b05030, 2018.

Ginoux, P., Prospero, J., Torres, O., and Chin, M.: Long-term simulation of global dust distribution with the GOCART model: correlation with North Atlantic Oscillation, Environ. Modell. Softw., 19, 113-128,doi: 10.1016/s1364-8152(03)00114-2, 2004.

Gonçalves Ageitos, M., Obiso, V., Miller, R. L., Jorba, O., Klose, M., Dawson, M., Balkanski, Y., Perlwitz, J., Basart, S., Di Tomaso, E., Escribano, J., Macchia, F., Montané, G., Mahowald, N. M., Green, R. O., Thompson, D. R., and Pérez García-Pando, C.: Modeling dust mineralogical composition: sensitivity to soil mineralogy atlases and their expected climate impacts, Atmos. Chem. Phys., 23, 8623-8657,doi: 10.5194/acp-23-8623-2023, 2023.

Guenther, A. B., Jiang, X., Heald, C. L., Sakulyanontvittaya, T., Duhl, T., Emmons, L. K., and Wang, X.: The Model of Emissions of Gases and Aerosols from Nature version 2.1 (MEGAN2.1): an extended and updated framework for modeling biogenic emissions, Geosci. Model Dev., 5, 1471-1492,doi: 10.5194/gmd-5-1471-2012, 2012.

Hamilton, D., Scanza, R., Yan, F., Guinness, J., Kok, J., Longlei, L., Xiaohong, L., Rathod, S., Jessica, S. W., Mingxuan, W., and Mahowald, N.: Improved methodologies for Earth system modelling of atmospheric soluble iron and observation comparisons using the Mechanism of Intermediate complexity for Modelling Iron (MIMI v1.0), Geosci. Model Dev., 12, 3835-3862,doi: 10.5194/GMD-12-3835-2019, 2019.

Hoesly, R. M., Smith, S. J., Feng, L. Y., Klimont, Z., Janssens-Maenhout, G., Pitkanen, T., Seibert, J. J., Vu, L., Andres, R. J., Bolt, R. M., Bond, T. C., Dawidowski, L., Kholod, N., Kurokawa, J., Li, M., Liu, L., Lu, Z. F., Moura, M. C. P., O'Rourke, P. R., and Zhang, Q.: Historical (1750-2014) anthropogenic emissions of reactive gases and aerosols from the Community Emissions Data System (CEDS), Geosci. Model Dev., 11, 369-408,doi: 10.5194/gmd-11-369-2018, 2018.

Hu, L., Millet, D. B., Baasandorj, M., Griffis, T. J., Turner, P., Helmig, D., Curtis, A. J., and Hueber, J.: Isoprene emissions and impacts over an ecological transition region in the U.S. Upper Midwest inferred from tall tower measurements, J Geophys Res-Atmos, 120, 3553-3571,doi: 10.1002/2014jd022732, 2015.

Lelieveld, J., Gromov, S., Pozzer, A., and Taraborrelli, D.: Global tropospheric hydroxyl distribution, budget and reactivity, Atmos. Chem. Phys., 16, 12477-12493,doi: 10.5194/acp-16-12477-2016, 2016.

Lewis, E. and Schwartz, S.: Sea salt aerosol production: Mechanisms, methods, measurements and models—A critical review, Washington DC American Geophysical Union Geophysical Monograph Series, 152, 3719,doi: 10.1029/GM152, 2004.

Li, W. S., Qi, Y. X., Liu, Y. C., Wu, G. R., Zhang, Y. J., Shi, J. H., Qu, W. J., Sheng, L. F., Wang, W. C., Zhang, D. Z., and Zhou, Y.: Daytime and nighttime aerosol soluble iron formation in clean and slightly polluted moist air in a coastal city in eastern China, Atmos. Chem. Phys., 24, 6495-6508,doi: 10.5194/acp-24-6495-2024, 2024.

Liu, X., Qu, H., Huey, L. G., Wang, Y., Sjostedt, S., Zeng, L., Lu, K., Wu, Y., Hu, M., Shao, M., Zhu, T., and Zhang, Y.: High levels of daytime molecular chlorine and nitryl chloride at a rural site on the North China Plain, Environ. Sci. Technol., 51, 9588-9595,doi: 10.1021/acs.est.7b03039, 2017.

https://doi.org/10.5194/egusphere-2026-1330
Preprint. Discussion started: 18 March 2026

Luo, C., Mahowald, N., Bond, T., Chuang, P. Y., Artaxo, P., Siefert, R., Chen, Y., and Schauer, J.: Combustion iron distribution and deposition, Glob. Biogeochem. Cycle, 22, GB1012,doi: 10.1029/2007gb002964, 2008.

M. S. Johnson and Meskhidze, N.: Atmospheric dissolved iron deposition to the global oceans: effects of oxalate-promoted Fe dissolution, photochemical redox cycling, and dust mineralogy, Geosci. Model Dev., 6, 1137-1155,doi: 10.5194/gmd-6-1137-2013, 2013.

Mahowald, N. M., Engelstaedter, S., Luo, C., Sealy, A., Artaxo, P., Benitez-Nelson, C., Bonnet, S., Chen, Y., Chuang, P. Y., Cohen, D. D., Dulac, F., Herut, B., Johansen, A. M., Kubilay, N., Losno, R., Maenhaut, W., Paytan, A., Prospero, J. M., Shank, L. M., and Siefert, R. L.: Atmospheric iron deposition: global distribution, variability, and human perturbations, ACS Earth Space Chem., 1, 245-278,doi: 10.1146/annurev.marine.010908.163727, 2009.

Meskhidze, N., Chameides, W. L., and Nenes, A.: Dust and pollution: A recipe for enhanced ocean fertilization?, J Geophys Res-Atmos, 110, D03301,doi: 10.1029/2004jd005082, 2005.

Myriokefalitakis, S., Ito, A., Kanakidou, M., Nenes, A., Krol, M., Mahowald, N., Scanza, R., Hamilton, D., Matthew, S. J., Meskhidze, N., Kok, J., Guieu, C., Baker, A., Jickells, T., Sarin, M., Bikkina, S., Shelley, R., Bowie, A., Morgane, M. G. P., and Duce, R.: Reviews and syntheses: the GESAMP atmospheric iron deposition model intercomparison study, Biogeosciences, 15, 6659-6684,doi: 10.5194/BG-15-6659-2018, 2018.

Nickovic, S., Vukovic, A., Vujadinovic, M., Djurdjevic, V., and Pejanovic, G.: Technical Note: High-resolution mineralogical database of dust-productive soils for atmospheric dust modeling, Atmos. Chem. Phys., 12, 845-855,doi: 10.5194/acp-12-845-2012, 2012.

Pakkattil, A. and Ghude, S.: Tropospheric ozone precursors over the Indian region: Insights into the shift toward a highly NOx-limited regime, Atmos. Environ., 353, 121233,doi: 10.1016/j.atmosenv.2025.121233, 2025.

Paris, R., Desboeufs, K. V., Formenti, P., Nava, S., and Chou, C.: Chemical characterisation of iron in dust and biomass burning aerosols during AMMA-SOP0/DABEX: implication for iron solubility, Atmos. Chem. Phys., 10, 4273-4282,doi: 10.5194/acp-10-4273-2010, 2010.

Philip, S., Martin, R. V., Snider, G., Weagle, C. L., van Donkelaar, A., Brauer, M., Henze, D. K., Klimont, Z., Venkataraman, C., Guttikunda, S. K., and Zhang, Q.: Anthropogenic fugitive, combustion and industrial dust is a significant, underrepresented fine particulate matter source in global atmospheric models, Environ. Res. Lett., 12, 044018,doi: 10.1088/1748-9326/aa65a4, 2017.

Priestley, M., le Breton, M., Bannan, T. J., Worrall, S. D., Bacak, A., Smedley, A. R. D., Reyes-Villegas, E., Mehra, A., Allan, J., Webb, A. R., Shallcross, D. E., Coe, H., and Percival, C. J.: Observations of organic and inorganic chlorinated compounds and their contribution to chlorine radical concentrations in an urban environment in northern Europe during the wintertime, Atmos. Chem. Phys., 18, 13481-13493,doi: 10.5194/acp-18-13481-2018, 2018.

Rawat, P. and Naja, M.: Remote sensing study of ozone, NO_2, and CO: some contrary effects of SARS-CoV-2 lockdown over India, Environ. Sci. Pollut. Res., 29, 22515-22530,doi: 10.1007/s11356-021-17441-2, 2022.

Rodríguez, S., Prospero, J. M., López-Darias, J., García-Alvarez, M.-I., Zuidema, P., Nava, S., Lucarelli, F., Gaston, C. J., Galindo, L., and Sosa, E.: Tracking the changes of iron solubility and air pollutants traces as African dust transits the Atlantic in the Saharan dust outbreaks, Atmos. Environ., 246, 118092,doi: 10.1016/j.atmosenv.2020.118092, 2021.

Scanza, R., Hamilton, D., García-Pando, C. P., Buck, C., Baker, A., and Mahowald, N.: Atmospheric processing of iron in mineral and combustion aerosols: development of an intermediate-complexity mechanism suitable for Earth system models, Atmos. Chem. Phys., 18, 14175-14196,doi: 10.5194/ACP-18-14175-2018, 2018.

Scanza, R. A., Mahowald, N., Ghan, S., Zender, C. S., Kok, J. F., Liu, X., Zhang, Y., and Albani, S.: Modeling dust as component minerals in the Community Atmosphere Model: development of framework and impact on radiative forcing, Atmos. Chem. Phys., 15, 537-561,doi: 10.5194/acp-15-537-2015, 2015.

Shao, Y., Wyrwoll, K.-H., Chappell, A., Huang, J., Lin, Z., McTainsh, G. H., Mikami, M., Tanaka, T. Y., Wang, X., and Yoon,

https://doi.org/10.5194/egusphere-2026-1330
Preprint. Discussion started: 18 March 2026

S.: Dust cycle: An emerging core theme in earth system science, Aeolian Res., 2, 181-204,doi: 10.1016/j.aeolia.2011.02.001, 2011.

Simpson, W. R., Brown, S. S., Saiz-Lopez, A., Thornton, J. A., and von Glasow, R.: Tropospheric halogen hhemistry: Sources, cycling, and impacts, Chem. Rev., 115, 4035-4062,doi: 10.1021/cr5006638, 2015.

Srinivas, B., Sarin, M. M., and Rengarajan, R.: Atmospheric transport of mineral dust from the Indo-Gangetic Plain: Temporal variability, acid processing, and iron solubility, Geochem. Geophys. Geosyst., 15, 3226-3243,doi: 10.1002/2014gc005395, 2014.

Stettler, M. E. J., Eastham, S., and Barrett, S. R. H.: Air quality and public health impacts of UK airports. Part I: Emissions, Atmos. Environ., 45, 5415-5424,doi: 10.1016/j.atmosenv.2011.07.012, 2011.

Sun, Y. H., Xu, L., Li, J. L., Li, K., Tchinda, N. T., and Du, L.: Role of atomic chlorine in atmospheric volatile organic compound oxidation and secondary organic aerosol formation: a review, Environmental Science-Atmospheres,doi: 10.1039/d5ea00101c, 2025.

Takahashi, Y., Higashi, M., Furukawa, T., and Mitsunobu, S.: Change of iron species and iron solubility in Asian dust during the long-range transport from western China to Japan, Atmos. Chem. Phys., 11, 11237-11252,doi: 10.5194/acp-11-11237-2011, 2011.

Tang, W., Llort, J., Weis, J., Perron, M. M. G., Basart, S., Li, Z., Sathyendranath, S., Jackson, T., Sanz Rodriguez, E., Proemse, B. C., Bowie, A. R., Schallenberg, C., Strutton, P. G., Matear, R., and Cassar, N.: Widespread phytoplankton blooms triggered by 2019 – 2020 Australian wildfires, Nature, 597, 370-375,doi: 10.1038/s41586-021-03805-8, 2021.

van Herpen, M., Li, Q. Y., Saiz-Lopez, A., Liisberg, J. B., Röckmann, T., Cuevas, C. A., Fernandez, R. P., Mak, J. E., Mahowald, N. M., Hess, P., Meidan, D., Stuut, J. B. W., and Johnson, M. S.: Photocatalytic chlorine atom production on mineral dust-sea spray aerosols over the North Atlantic, Proc. Natl. Acad. Sci. U. S. A., 120, e2303974120,doi: 10.1073/pnas.2303974120, 2023.

Wang, T., Tang, J., Sun, M., Liu, X., Huang, Y., Huang, J., Han, Y., Cheng, Y., Huang, Z., and Li, J.: Identifying a transport mechanism of dust aerosols over South Asia to the Tibetan Plateau: A case study, Sci. Total Environ., 758, 143714,doi: 10.1016/j.scitotenv.2020.143714, 2021a.

Wang, W. C., Luo, C. H., Sheng, L. F., Zhao, C. F., Zhou, Y., and Chen, Y. H.: Effects of biomass burning on chlorophyll-a concentration and particulate organic carbon in the subarctic North Pacific Ocean based on satellite observations and WRF-Chem model simulations: A case study, Atmos. Res., 254, 105526,doi: 10.1016/j.atmosres.2021.105526, 2021b.

Wang, X., Jacob, D. J., Fu, X., Wang, T., Breton, M. L., Hallquist, M., Liu, Z., McDuffie, E. E., and Liao, H.: Effects of anthropogenic chlorine on $PM_{2.5}$ and ozone air quality in China, Environ. Sci. Technol., 54, 9908-9916,doi: 10.1021/acs.est.0c02296, 2020.

Wittmer, J. and Zetzsch, C.: Photochemical activation of chlorine by iron-oxide aerosol, J. Atmos. Chem., 74, 187-204,doi: 10.1007/s10874-016-9336-6, 2017.

Wittmer, J., Bleicher, S., and Zetzsch, C.: Iron(III)-induced activation of chloride and bromide from modeled salt pans, J. Phys. Chem. A, 119, 4373-4385,doi: 10.1021/jp508006s, 2015a.

Wittmer, J., Bleicher, S., Ofner, J., and Zetzsch, C.: Iron(III)-induced activation of chloride from artificial sea-salt aerosol, Environ. Chem., 12, 461-475,doi: 10.1071/en14279, 2015b.

Wu, C., Lin, Z., Liu, X., Ji, D., Zhang, H., Li, C., and Lin, G.: Description of dust emission parameterization in CAS - ESM2 and its simulation of global dust cycle and East Asian dust events, J. Adv. Model. Earth Syst., 13, e2020MS002456,doi: 10.1029/2020ms002456, 2021.

Wu, S. C., Kumar, R., Li, P. Y., Kotamarthi, R., Collis, S., Shams, S., and Sharma, A.: Sensitivity of regional WRF-Chem air quality and weather simulations to biomass-burning emission data sets: A case study of the impact of canadian wildfire on the US, J Geophys Res-Atmos, 130, e2025JD043944,doi: 10.1029/2025jd043944, 2025.

https://doi.org/10.5194/egusphere-2026-1330
Preprint. Discussion started: 18 March 2026

Xia, X., Zong, X., Cong, Z., Chen, H., Kang, S., and Wang, P.: Baseline continental aerosol over the central Tibetan plateau and a case study of aerosol transport from South Asia, Atmos. Environ., 45, 7370-7378,doi: 10.1016/j.atmosenv.2011.07.067, 2011.

Yang, J., Kang, S., Hu, Y., Chen, X., and Rai, M.: Influence of south Asian biomass burning on ozone and aerosol concentrations over the Tibetan Plateau, Adv. Atmos. Sci., 39, 1184-1197,doi: 10.1007/s00376-022-1197-0, 2022.

Yin, S., Yi, X., Li, L., Huang, L., Ooi, M. C. G., Wang, Y., Allen, D. T., and Streets, D. G.: An updated anthropogenic emission inventory of reactive chlorine precursors in China, ACS Earth Space Chem., 6, 1846-1857,doi: 10.1021/acsearthspacechem.2c00096, 2022.

Zan, J., Maher, B. A., Fang, X., Stevens, T., Ning, W., Wu, F., Yang, Y., Kang, J., and Hu, Z.: Global dust impacts on biogeochemical cycles and climate, Nat. Rev. Earth Environ., 6, 789-807,doi: 10.1038/s43017-025-00734-2, 2025.

Zender, C. S., Bian, H., and Newman, D.: Mineral Dust Entrainment and Deposition (DEAD) model: Description and 1990s dust climatology, J Geophys Res-Atmos, 108, 4416,doi: 10.1029/2002jd002775, 2003.

Zhang, B., Shen, H., Yun, X., Zhong, Q., Henderson, B. H., Wang, X., Shi, L., Gunthe, S. S., Huey, L. G., Tao, S., Russell, A. G., and Liu, P.: Global emissions of hydrogen chloride and particulate chloride from continental sources, Environ. Sci. Technol., 56, 3894-3904,doi: 10.1021/acs.est.1c05634, 2022.

Zhang, H., Li, R., Dong, S., Wang, F., Zhu, Y., Meng, H., Huang, C., Ren, Y., Wang, X., Hu, X., Li, T., Peng, C., Zhang, G., Xue, L., Wang, X., and Tang, M.: Abundance and fractional solubility of aerosol iron during winter at a coastal city in Northern China: Similarities and contrasts between fine and coarse particles, J Geophys Res-Atmos, 127, e2021JD036070,doi: 10.1029/2021jd036070, 2021.

Zhang, H., Li, R., Huang, C., Li, X., Dong, S., Wang, F., Li, T., Chen, Y., Zhang, G., Ren, Y., Chen, Q., Huang, R.-j., Chen, S., Xue, T., Wang, X., and Tang, M.: Seasonal variation of aerosol iron solubility in coarse and fine particles at an inland city in northwestern China, Atmos. Chem. Phys., 23, 3543-3559,doi: 10.5194/acp-23-3543-2023, 2023.

Zhang, T. L. and Zheng, M.: Atmospheric iron in Chinese marginal seas and the Northwest Pacific: A review, China Environ. Sci., 44, 602-619, 2024.

Zhang, Z., Tao, J., Zhang, L., Hu, B., Liu, M., Nie, F., Lu, H., Chen, L., Wu, Y., Chen, D., Wang, B., and Che, H.: Influence of sources and atmospheric processes on metal solubility in $PM_{2.5}$ in urban Guangzhou, South China, Sci. Total Environ., 951, 175807,doi: 10.1016/j.scitotenv.2024.175807, 2024.

Zhi, M. K., Wang, G. C., Xu, L., Li, K. L., Nie, W., Niu, H. Y., Shao, L. Y., Liu, Z. R., Yi, Z. W., Wang, Y. T., Shi, Z. B., Ito, A., Zhai, S. X., and Li, W. J.: How acid iron dissolution in aged dust particles responds to the buffering capacity of carbonate minerals during Asian dust storms, Environ. Sci. Technol., 6167-6178,doi: 10.1021/acs.est.4c12370, 2025.

Zhu, Y., Li, W., Lin, Q., Yuan, Q., Liu, L., Zhang, J., Zhang, Y., Shao, L., Niu, H., Yang, S., and Shi, Z.: Iron solubility in fine particles associated with secondary acidic aerosols in east China, Environ. Pollut., 264, 114769,doi: 10.1016/j.envpol.2020.114769, 2020.